The Leading Edge®

Special Section: Microseismic

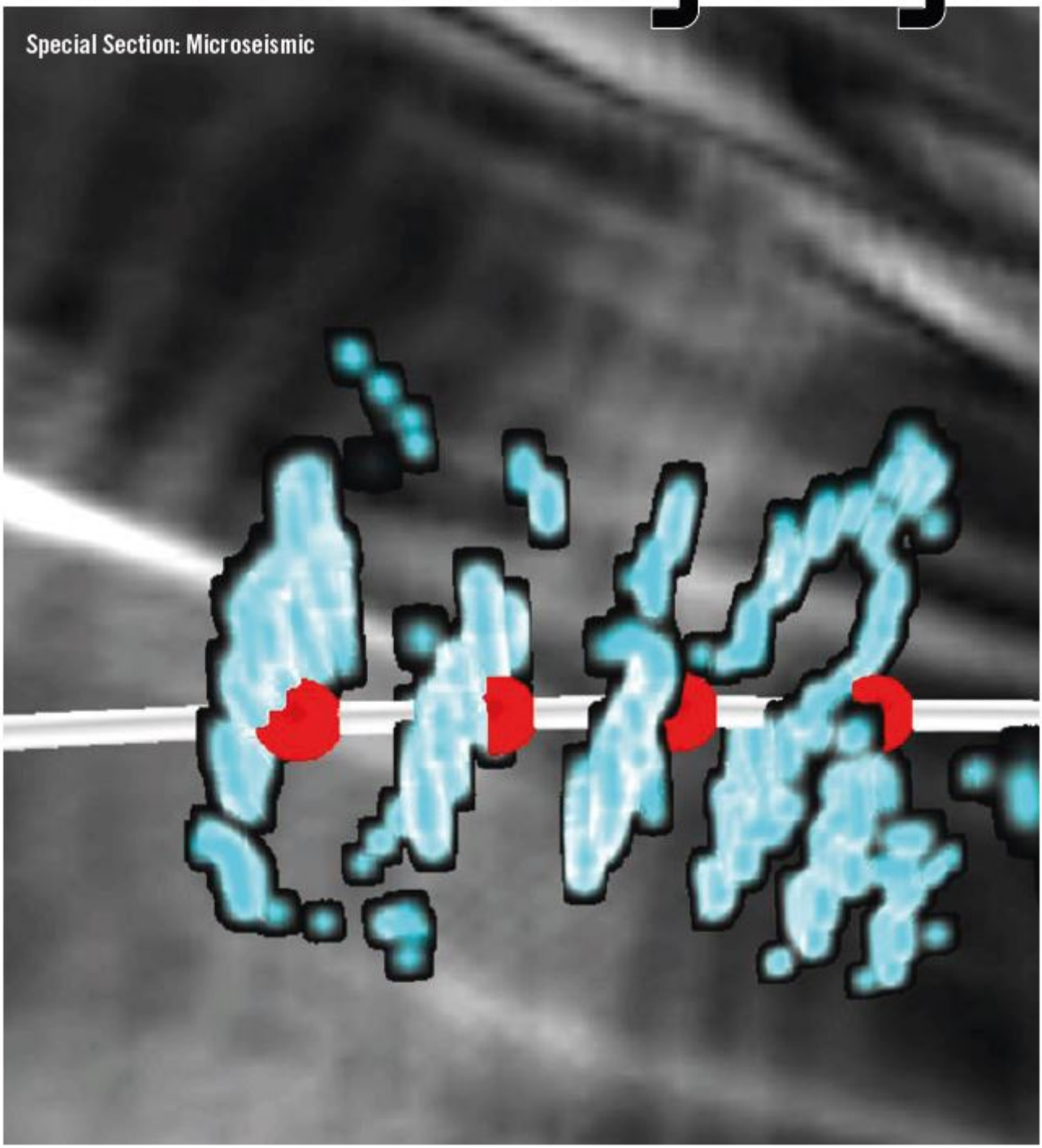

SEG SOCIETY OF EXPLORATION GEOPHYSICISTS

October 2017 · Volume 36, No.10
ISSN 1070-485X

High-resolution microseismic imaging

Vladimir Grechka[1], Zhao Li[2], Bo Howell[2], Hugo Garcia[3], and Tom Wooltorton[3]

Abstract

We examine the feasibility of high-resolution microseismic imaging of unconventional reservoirs. Given frequencies in typical downhole microseismic data that are almost an order of magnitude higher than in seismic reflection data, a comparable increase in image resolution might be expected, bringing potential resolution of downhole microseismic images to a few meters. We demonstrate that such a resolution is indeed achievable and present two case studies illustrating the reservoir features that can be imaged. Our first example, constructed with P-waves recorded in the Woodford Field, reveals internal fabric of the Woodford reservoir and formations surrounding it, allowing us to discriminate the stimulated and unstimulated zones of the Lower Woodford Shale. Encouraged by those results, in our second example, this time from the Bakken Field, we use the slow shear waves, which are more sensitive to fluids than P-waves, to find out whether hydraulic fractures themselves could be imaged. Our seismic volume contains peculiar geobodies, growing precisely from perforation holes spaced at a 40 ft interval in a treatment well landed in the Middle Bakken. These geobodies penetrate through the Lower Bakken Shale reservoir and terminate at the top of the Three Forks dolomites. While our interpretation of the extracted geobodies as hydraulic fractures remains an interpretation, the remarkably high resolution of seismic images obtained in both case studies is unquestionable.

Introduction

Microseismic technology, as applied in the oil industry today, focuses on the characterization of seismic sources: the traveltimes of direct waves excited by a microseismic event yield the source location, and the recorded wave amplitudes provide information about the source dynamics expressed by its seismic moment tensor. Practitioners, however, know that direct waves are always accompanied by scattered codas (e.g., Figures 2 and 6) — the subsurface response to a microseismic source. Although reflected, refracted, and head waves identified in codas have been used to improve the description of microseismic sources (Rutledge and Soma, 2013; Belayouni et al., 2015, 2017; Daniel et al., 2016), here we are not interested in dissecting the coda into its constituents. Instead, we take the entire coda and project it back into a reservoir to illuminate its internal structure and possibly image stimulation-induced hydraulic fractures.

Microseismic imaging is hardly a new idea, as both modeling studies (e.g., Lin and Zhang, 2016; Zhu and Sun, 2016) and field applications (Block et al., 1994; House et al., 1997; Dyer et al., 2008; Reshetnikov et al., 2010, 2015; Cole et al., 2015) have been published. Yet microseismic images found in the literature are often unsatisfactory, appearing artifact-laden and poorly focused (Figure 2 in House et al., 1997; Figure 8 in Dyer et al., 2008; Figure 4 in Reshetnikov et al., 2010; Figure 5 in Cole et al., 2015; Figure 8 in Reshetnikov et al., 2015), exactly as one would expect because of sparsity of downhole sensors and irregular spatial distribution of sources of naturally occurring microseismic events. To suppress imaging artifacts, Reshetnikov et al. (2015) applied the Fresnel-volume prestack depth migration (Lüth et al., 2005; Buske et al., 2009) that proved to be helpful but fell short of producing high-quality images. Here, we take the next logical step and postprocess our migrated volumes to extract attributes, such as local dips, azimuths, and discontinuities (see Barnes, 2016, for their definitions), useful for subsequent interpretation.

We begin the paper with a discussion of challenges faced by microseismic imaging to help the reader appreciate the difficulties preventing widespread application of this familiar-for-geophysicists technology to unconventional reservoirs. Then we proceed with a detailed description of our Woodford and Bakken case studies, highlighting the choices made and analyzing the geologic and reservoir-stimulation information that has been provided by microseismic images.

Technical challenges of microseismic imaging

The first challenge, well documented in the literature of microseismic imaging, is irregular spatial distribution of natural passive sources and sparse distribution of downhole receivers (e.g., black dots and blue triangles in Figure 1) as opposed to regular distribution of active sources and receivers in seismic reflection surveys, designed with a certain imaging objective in

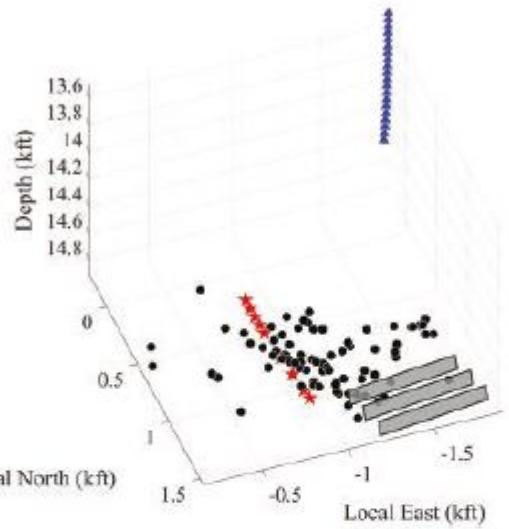

Figure 1. Microseismic recording geometry and events. The stars, triangles, and dots indicate perforation shots in a nearly horizontal well landed in the Lower Woodford, 3C sensors in a single vertical well, and microseismic events selected for imaging, respectively. The transparent rectangles are approximately east-west-oriented hydraulic fractures suggested by the attribute volume in Figure 4.

[1]Marathon Oil Company.
[2]Borehole Seismic LLC.
[3]GeoTeric.

https://doi.org/10.1190/tle36100822.1.

mind (Vermeer, 2012). As mentioned in the Introduction, we attenuate imaging artifacts, caused by the sparsity and irregularity of microseismic data, through postprocessing of migrated volumes, aimed at enhancing the interpretable content of images.

The second challenge is the variability of focal mechanisms of microseismic events as opposed to the uniformity of active seismic sources — the variability causing a point in the subsurface to be illuminated by waves with opposite polarities excited by different passive sources. Such a polarity disparity, which tends to cancel out useful contributions of different sources to image, is obviously detrimental to the image quality. One way to deal with this problem is through moment tensor inversion, making it possible to either consistently flip polarities, enforcing their uniformity, or select microseismic events that have similar moment tensors and illuminate a desired subsurface volume with waves of the same polarity. We select the latter option for our Bakken case study and resort to brute-force polarity equalization — squaring the instantaneous phase of recorded seismic traces treated as analytic signals (Barnes, 2016, chapter 4) — for our Woodford data.

The third challenge has to do with the requirement of having a precise velocity model for constructing the microseismic image, its precision estimated based on the following consideration: velocity-model errors greater than one-half of the dominant period of microseismic data are going to result in stacking the data with opposite polarities when the data are back-projected into the subsurface to form its image, invariably blurring and smearing the image. For example, a velocity model for data that have the dominant frequency around 250 Hz (such as that in Figures 2a and 2b) should have the precision no worse than 2 ms when the phase of data is not squared and no worse than 1 ms when the phase is squared because squaring the phase approximately doubles the dominant frequency. Conversely, microseismic records can be low-pass filtered to make one-half of their resulting dominant period exceed a given velocity-model error, an undesirable process tending to reduce the image resolution.

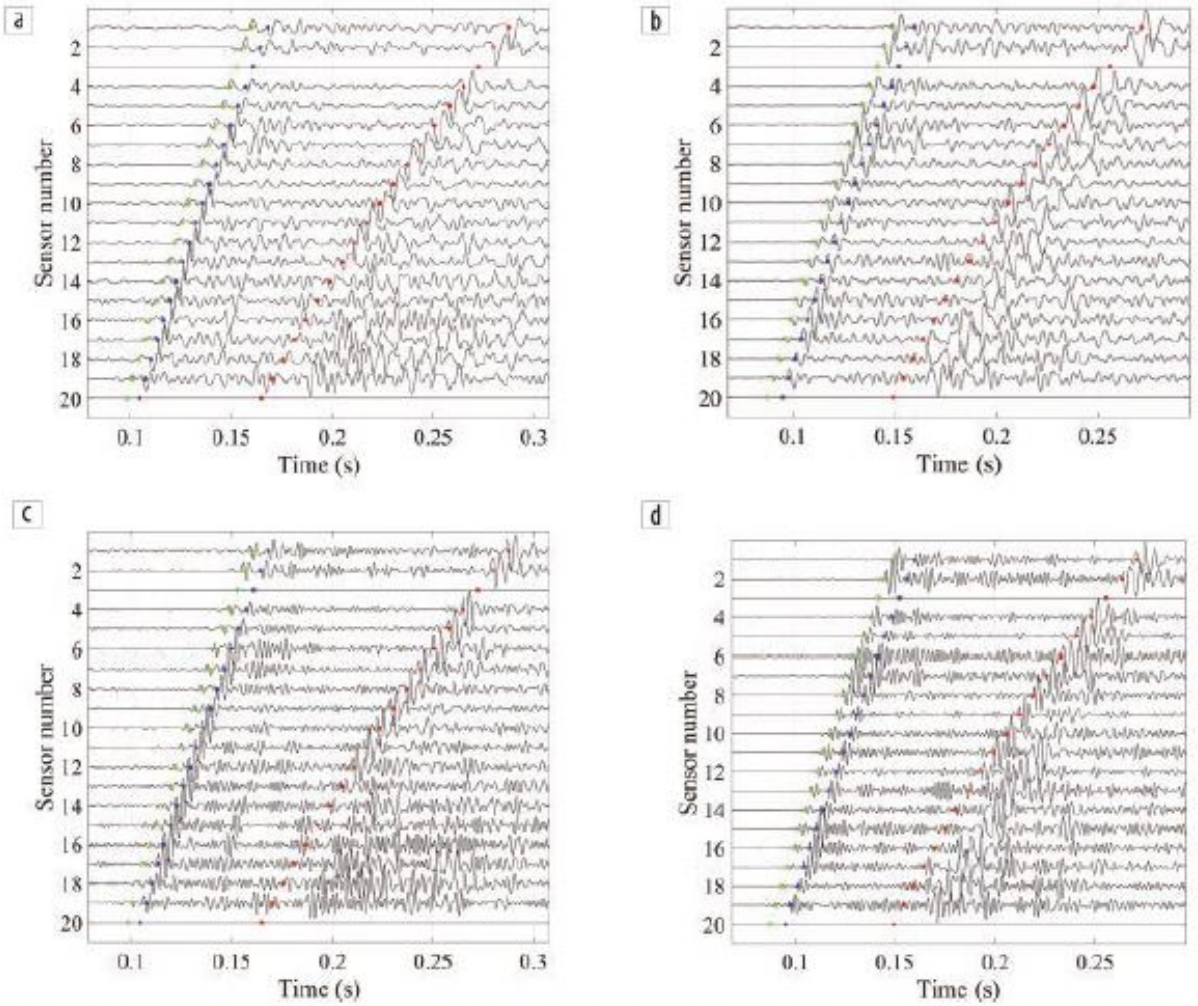

Figure 2. Vertical components of two representative microseismic events (a) and (b) before and (c) and (d) after squaring the phase of seismic traces. Every trace is normalized individually for optimal quality of the display. The green, blue, and red dots mark traveltimes of the direct P-waves, interpreted P-wave reflections from the Woodford–Hunton interface, and the direct S-waves, respectively. Those traveltimes have been computed in a layered anisotropic model described in Belayouni et al. (2017).

Woodford case study

We begin our examples with a data set acquired in the Woodford Field by a string of three-component (3C) sensors deployed in a single monitor well (Figure 1) and processed for the standard microseismic deliverable — a catalog of event hypocenters. Out of a full catalog containing 317 events with variable signal-to-noise ratios (S/N), we select 80 strong events (black dots in Figure 1) for imaging, the events recorded during two last (heel) hydraulic stimulation stages, closest to the monitor well. Our choice to decimate the available microseismic catalog expresses our reluctance to let relatively high noise in low S/N events adversely influence an image. Another choice made in our two case studies is to apply conventional 3D prestack Kirchhoff depth migration to the vertical component of recorded data instead of 3D vector Kirchhoff migration (Wang, 2004; Lüth et al., 2005) to 3C data — the choice acknowledging unknown-at-present benefits of vector migration for microseismic imaging and the desirability to mitigate the propagation of errors in sensor orientation to the migrated volumes.

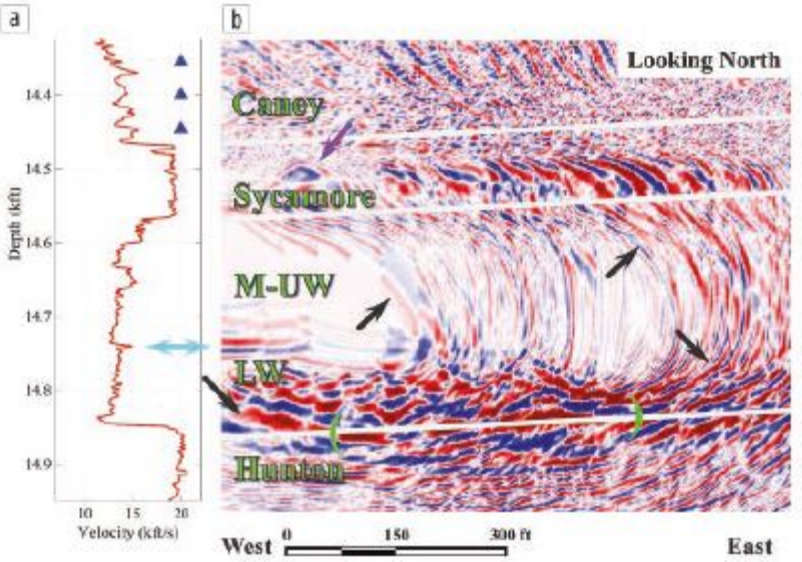

Figure 3. (a) P-wave sonic log and (b) west-east vertical section through seismic image volume. The gray lines (dipping at 2.5° from northeast to southwest) are interfaces of homogeneous layers comprising the velocity model (Belayouni et al., 2017) used for imaging. The abbreviations M-UW and LW stand for the Middle-Upper Woodford and the Lower Woodford. The hole in the western part of the image, at depths between approximately 14.55 kft and 14.75 kft, is caused by restricting the lateral migration aperture to ±150 ft from the vertical plane passing through a source-receiver pair. The blue triangles indicate the depths of the bottom three sensors of the receiver string displayed in Figure 1.

All 80 events selected for imaging (same as those discussed in Belayouni et al., 2017) contain arrivals, marked with blue dots in Figures 2a and 2b, that were interpreted as the P-wave reflections from the Hunton Formation underlying the Woodford (Figure 3) and proved to be instrumental in improving precision of the computed event hypocenters (see Belayouni et al., 2017, for details). Figures 2a and 2b make it clear that each of the direct P-waves, their modeled times shown with green dots, excites a long coda (or reverberation) rather than a single reflection, the coda likely overlapping in time with the coda excited by the direct S-wave. We use the entire coda, understood as the subsurface response to a microseismic source, to image the subsurface. A close examination of Figures 2a and 2b reveals the opposite polarities of the direct P-wave arrivals of our two selected events, a common feature of microseismic data, degrading the quality of migration if not destroying an image altogether. To equalize polarity across the data set, we square the phase of data, achieving the desired outcome (Figures 2c and 2d) at an unfortunate price of altering the recorded amplitudes and making it impossible to obtain a true-amplitude image.

We utilize the P-wave portion of the seismic velocity model, containing a mixture of isotropic, vertically transversely isotropic, and orthorhombic layers (Figure 4 in Belayouni et al., 2017) and fitting our time picks with the root-mean-square (rms) misfit of 0.86 ms (Figure 6 in Belayouni et al., 2017) to compute a traveltime table for prestack Kirchhoff depth migration. Then we migrate the squared-phase traces (such as those in Figures 2c and 2d) and output the P-wave image volume on a 5 × 5 × 5 ft grid. A vertical slice through the volume presented in Figure 3 exhibits the expected imaging artifacts, some of them indicated with black arrows; but also, promisingly, it displays a number of sonic-log-corroborated and geologically interpretable features. We mention the following:

- About a 400 ft long portion of the Woodford-Hunton interface (marked by green parentheses in Figure 3) is well imaged; in fact, the top Hunton reflector is so strong that the image has been clipped to make its other features visible.
- The high-velocity, about 8 ft thick layer (cyan arrow) in the Woodford, separating the reservoir into the Middle-Upper and Lower units, is present in the image, attesting to the obtained resolution.
- Images of the Middle-Upper and Lower Woodford formations exhibit different textures, suggesting a potential relationship to the formations' geology: the Upper Woodford is chert-rich, whereas the Lower Woodford is shale-rich.
- The purple arrow indicates an anticline in the carbonate Sycamore Formation, a part of a karst structure that will become apparent in Figure 4. Also, the character of the image of the Sycamore Formation differs from those of the adjacent formations.

Even though Figure 3 lends itself to geologic interpretation, removing artifacts from the image should make the interpretation more straightforward. With this goal in mind, we extract the local dip and azimuth attributes from the original image volume and display them as a color blend in Figure 4. Our dip

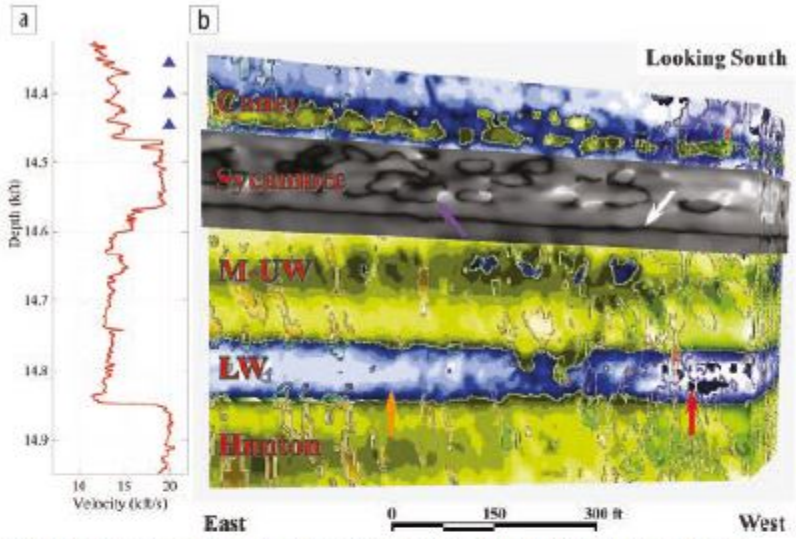

Figure 4. (a) P-wave sonic log and (b) color blend of the local dip and azimuth attributes extracted from the migrated volume in Figure 3. The black-and-white inset displays the dip attribute only.

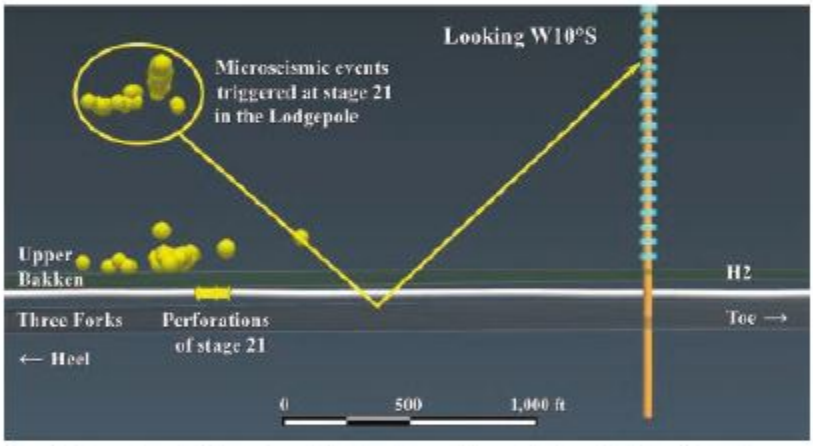

Figure 5. Lodgepole events (yellow spheres inside the yellow oval) triggered at stage 21 of hydraulic fracturing of well H2 and used to construct the microseismic image in Figure 7. The event cluster in the oval is located approximately 900 ft above the stimulated well H2. The Upper Bakken and Three Forks horizons mark the top and bottom of the Bakken reservoir. The cyan disks are 3C sensors deployed in the monitor well (orange) denoted as well #5 in Figure 1 in Dohmen et al. (2014) or as well B in Figure 6 in Grechka et al. (2016).

calculation utilizes a gradient structure tensor (Barnes, 2016, chapter 5) to determine the dominant structural orientation in the image volume by applying the calculation within a 3D spatial filter around each image point. The results are stored as a pair of 3D seismic volumes, capturing the local dip magnitude and the dip direction (azimuth) for each sample in the data. Those volumes are then combined according to a 2D color map in which the hue indicates the azimuth and the gray scale indicates the dip. If a subvertical wavefront crosses a formation boundary and refracts, the image structure inflects away from or toward the monitor well, exhibiting variation in orientation and, hence, the color, allowing the formation boundaries to be visually interpreted.

The features observed in Figure 3 become less ambiguous now in Figure 4. Specifically, the Middle-Upper and Lower Woodford units are clearly identifiable by their colors (greenish and bluish, respectively); the Sycamore-Woodford interface (white arrow) appears extremely sharp in the dip attribute only; and the previously unknown karst or mound structure in the Sycamore (purple arrow) becomes unmistakable (compare the black-and-white inset in Figure 4 with Figure 17 in Loucks, 1999, or with Figures 17 and 18 in Kumbalek, 2015).

To assess whether hydraulic fractures have any impact on the image, let us note that the western part of the stimulated Lower Woodford unit appears more broken (red arrow in Figure 4) than its eastern part (orange arrow). We attribute the difference to fractures opened at stages stimulated earlier, the fractures oriented approximately normally to the treated well (as schematically indicated by gray rectangles in Figure 1) and evident in a microseismic data set acquired at the earth's surface (not shown). Figure 4, hinting at a possibility of inferring hydraulic fractures from microseismic images, is the motivation for our next effort.

Bakken case study

We apply the same methodology to a data set acquired in the Bakken Field and discussed in Yang et al. (2013), Dohmen et al. (2014), Li et al. (2014), and Grechka et al. (2016) among other papers. For our purpose, we select 97 strong events triggered in the Lodgepole Formation (yellow spheres enclosed in the yellow oval in Figure 5) at treatment stage 21 of well H2 (Figure 1 in Dohmen et al., 2014), the records of waves excited by those events exhibiting long codas accompanying the direct S-waves, such as the one displayed in Figure 6. The vertical components of the direct S-waves recorded in several downhole microseismic surveys carried out in the Bakken Field correspond to the slow S-waves (Figures 3 and 4 in Grechka and Yaskevich, 2014, or Figure 7 in Grechka et al., 2016), expected to be sensitive to fluid-filled fractures and offering the possibility to image the fractures. Because the 97 events we use for imaging have similar moment tensors (some of them displayed in Figure 8 in Grechka et al., 2016) and exhibit consistent polarities on our records, we do not need to square the phase of data before migration.

The geometry in Figure 5 implies that our sensors (cyan disks) record reflected and scattered waves (schematically shown with the yellow arrow) from the reservoir zone stimulated prior to stage 21 because the event sources are located at the heel side of the stimulated well from the receivers. Keeping this geometry in mind, we migrate our microseismic data (Figure 6) in a layered anisotropic model that fits arrival-time picks of the direct P- and S-waves with the rms misfit of 1.3 ms (Grechka et al., 2016) and construct a slow shear-wave image volume containing the Bakken reservoir around the midpoint between the event cluster and the monitor well in Figure 5. Then, as before, we compute volumes of the local dip and azimuth attributes, this time followed by the extraction of discontinuities (Barnes, 2016, chapter 6) from those volumes.

The discontinuities, arranging themselves in elongated geobodies from 1 to 4 voxels (5 to 20 ft) wide, are displayed in cyan in Figure 7. Remarkably, the geobodies grow from the perforation holes (red circles) of stage 19, penetrate through the entire Lower Bakken Shale reservoir, and terminate precisely at the top of the Three Forks dolomites, suggesting the extracted geobodies to be hydraulic fractures opened by stimulation of stage 19. Although this is interpretation only and should be taken as such, any alternative would have to explain the regularity of spatial arrangement of the geobodies and their relationship to the perforations, something we find difficult without invoking hydraulic fractures.

The vertical slice through the migrated seismic volume in the background of Figure 7 hints at a possible origin of the imaged discontinuities — the sharp terminations of the brown and dark blue seismic phases (indicated by white arrows) at the leftmost perforation hole of stage 19. Additionally, Figure 8, which is a map view of the geobodies on the background of the dip attribute exhibiting a washboard pattern, suggests that the extracted geobodies, consistent with the fine-scale fabric of the Lower Bakken Shale, might highlight the zones of weakness in the shale prone to be fractured.

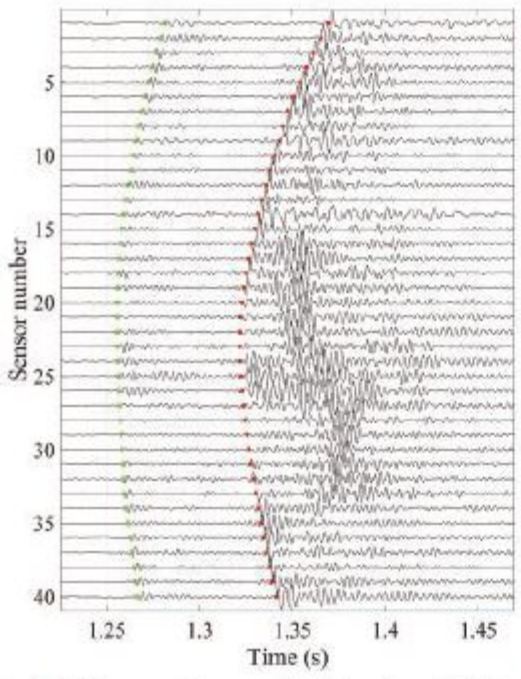

Figure 6. Vertical component of a representative Lodgepole event. As in Figure 2, the green and red dots indicate modeled times of the direct P- and S-waves, respectively.

Discussion and conclusions

Unconventional reservoirs, often too thin for surface reflection seismic to resolve their internal structures, are developed semiblindly today. Thousands of wells producing oil and gas are geosteered by logging while drilling, and data collected when completing the wells are primarily geared toward understanding a reservoir's fluid-flow properties rather than its geology. This is where microseismic monitoring comes in, helping to map the rock ruptures and infer a reservoir volume contributing to production. As currently practiced in the industry, however, microseismic is mostly about sources of microseismic events and much less about the formations surrounding them.

Our paper is an attempt to expand the application area of microseismic monitoring and make it a tool not only for characterizing the geometry and dynamics of seismic sources but also for imaging the subsurface around them at a resolution useful for

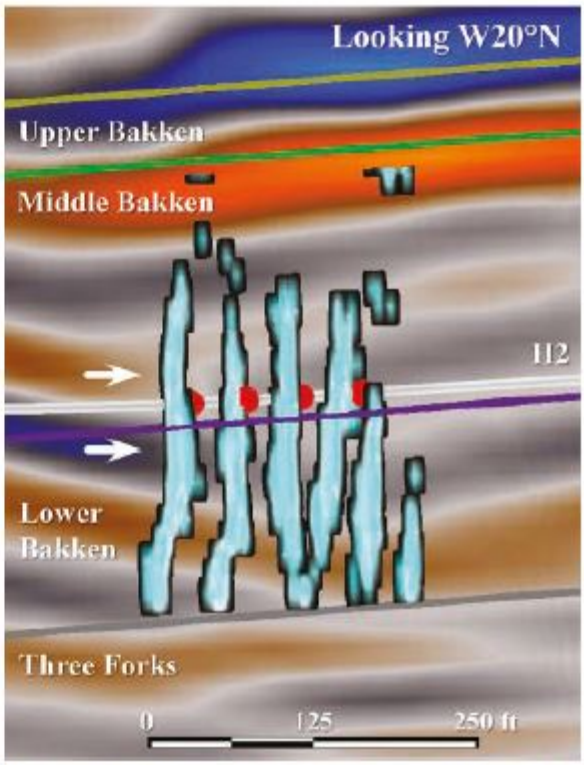

Figure 7. Discontinuities (cyan) extracted from volumes of local dip and azimuth attributes of the slow shear-wave image volume displayed in the background. The red circles indicate four perforation holes of stage 19 in well H2 placed at a 40 ft spacing. The Upper Bakken, Middle Bakken, Lower Bakken, and Three Forks tops are the interfaces in a layered velocity used to create the image.

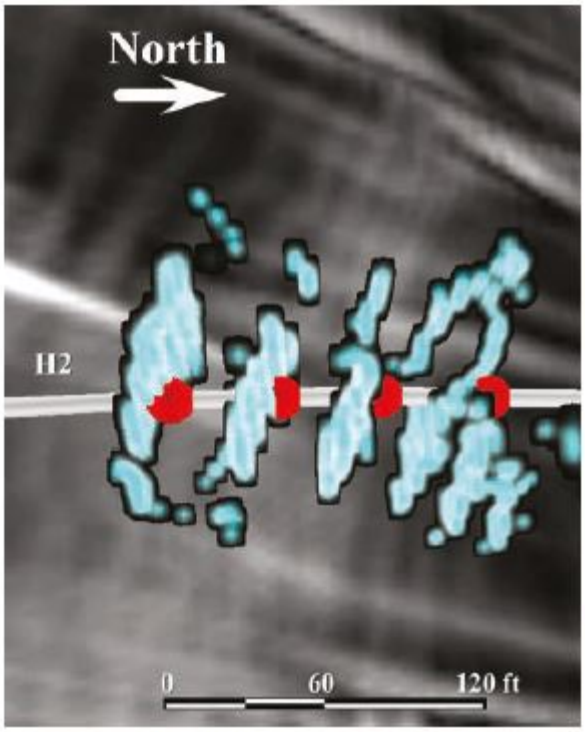

Figure 8. Map view of the geobodies (cyan) and perforation holes of stage 19 (red), same as those in Figure 7, on background of the local dip attribute.

field development. Even though we applied the most basic Kirchhoff migration, we have managed to obtain astonishing resolution of our attribute volumes. With this being demonstrated and providing enough encouragement to move the microseismic imaging technology forward, let us identify the existing gaps and contemplate how they might be filled.

In our opinion, it is critical to understand the details of the adverse influence of irregular spatial distributions of sources and sparse receiver geometries on microseismic images and offer remedies that could be implemented at the migration stage — that is, prior to attribute extraction. Full-waveform reverse time migration (RTM) of 3C data immediately comes to mind, as it would allow one to seamlessly merge the P- and S-wave images (such as those in Figure 3 and in the background of Figure 7, or in Figure 9 in Reshetnikov et al., 2015) and likely improve the quality of a combined image over the quality of individual ones. A competing option could be less expensive and more versatile than RTM Kirchhoff migration, superimposing (possibly polarity-corrected) P-, fast S-, and slow S-wave images in a single volume.

Another group of questions relates to determining the lowest S/N of microseismic events that should be included in imaging. We used only the high S/N events (such as those displayed in Figures 2 and 6), intentionally sacrificing the data quantity for quality, without knowing whether or not this is an optimal solution. An alternative view is that the power of the stack should suppress noise, and a larger event population should enhance the subsurface illumination. On the flip side of that argument though, hypocenters of low S/N events are expected to be less precise than hypocenters of high S/N events, diminishing the value of the former for imaging and, although qualitatively supporting the choice made in the paper, pointing to the desirability of having a formal event-selection criterion.

Finally, the presented case studies prove the feasibility of obtaining high-resolution microseismic images but leave the entire subject of making those images a part of a field-development program outside the scope of the paper. Clearly, the microseismic imaging technology is not ready for that yet, but its value can be realized only by making it routine and, upon reaching a desired level of confidence, beginning to use the subsurface images to influence decisions on well placements and completions. We believe this could happen in the future, as it has happened for conventional reservoirs, quite in line with British novelist Joseph Conrad's assertion that "seeing is everything." TLE

Acknowledgments

We thank Marathon Oil Company for permission to publish the paper and acknowledge Hess Corporation as the owner of the Bakken data set.

Corresponding author: vgrechka@marathonoil.com

References

Barnes, A. E., 2016, Handbook of poststack seismic attributes: SEG, Geophysical references series, no. 21, https://doi.org/10.1190/1.9781560803324.

Belayouni, N., A. Gesret, G. Daniel, and M. Noble, 2015, Microseismic event location using the first and reflected arrivals: Geophysics, **80**, no. 6, WC133–WC143, https://doi.org/10.1190/geo2015-0068.1.

Belayouni, N., D. A. Katz, V. Grechka, and P. Christianson, 2017, Microseismic event location with direct and reflected waves: A Woodford case study: 87th Annual International Meeting, SEG, Expanded Abstracts, 3981–3986, https://doi.org/10.1190/segam2017-16890707.1.

Block, L. V., C. H. Cheng, M. C. Fehler, and W. S. Phillips, 1994, Seismic imaging using microearthquakes induced by hydraulic fracturing: Geophysics, **59**, no. 1, 102–112, https://doi.org/10.1190/geo1992-0156.

Buske, S., S. Gutjahr, and C. Sick, 2009, Fresnel volume migration of single-component seismic data: Geophysics, **74**, no. 6, WCA47–WCA55, https://doi.org/10.1190/1.3223187.

Cole, S., M. Karrenbach, S. Roche, J. Gumble, L. LaFlame, M. Emuh, V. Yartsev, and B. Bartling, 2015, Interferometric imaging of microseismic data: 85th Annual International Meeting, SEG, Expanded Abstracts, 721–725, https://doi.org/10.1190/segam2015-5876692.1.

Daniel, G., E. Fortier, R. Romijn, and S. Oates, 2016, Location results from borehole microseismic monitoring in the Groningen gas reservoir, Netherlands: 6th Workshop on Passive Seismic, EAGE, Extended Abstracts, https://doi.org/10.3997/2214-4609.201600016.

Dohmen, T., J.-P. Blangy, and J. Zhang, 2014, Microseismic depletion delineation: Interpretation, **2**, no. 3, SG1–SG13, https://doi.org/10.1190/INT-2013-0164.1.

Dyer, B. C., U. Schanz, F. Ladner, M. O. Häring, and T. Spillman, 2008, Microseismic imaging of a geothermal reservoir stimulation: The Leading Edge, **27**, no. 7, 856–869, https://doi.org/10.1190/1.2954024.

Grechka, V., Z. Li, B. Howell, and V. Vavryčuk, 2016, Single-well moment tensor inversion of tensile microseismic events: Geophysics, **81**, no. 6, KS219–KS229, https://doi.org/10.1190/geo2016-0186.1.

Grechka, V., and S. Yaskevich, 2014, Azimuthal anisotropy in microseismic monitoring: A Bakken case study: Geophysics, **79**, no. 1, KS1–KS12, https://doi.org/10.1190/geo2013-0211.1.

House, L., W. S. Phillips, M. Fehler, and J. Rutledge, 1997, Using waveforms of induced microearthquakes to image hydraulic fracture systems: 67th Annual International Meeting, SEG, Expanded Abstracts, 234–237, https://doi.org/10.1190/1.1885871.

Kumbalek, M., 2015, Analysis of paleokarst sinkholes in the Arkoma Basin using 3-D seismic: Oil & Gas Exploration, **66**, no. 3, 158–175.

Li, J., C. Li, S. A. Morton, T. Dohmen, K. Katahara, and M. N. Toksöz, 2014, Microseismic joint location and anisotropic velocity inversion for hydraulic fracturing in a tight Bakken reservoir: Geophysics, **79**, no. 5, C111–C122, https://doi.org/10.1190/geo2013-0345.1.

Lin, Y., and H. Zhang, 2016, Imaging hydraulic fractures by microseismic migration for downhole monitoring system: 86th Annual International Meeting, SEG, Expanded Abstracts, 2672–2677, https://doi.org/10.1190/segam2016-13973310.1.

Loucks, R. G., 1999, Paleocave carbonate reservoirs: Origins, burial-depth modifications, spatial complexity, and reservoir implications: AAPG Bulletin, **83**, no. 11, 1795–1834.

Lüth, S., S. Buske, R. Giese, and A. Goertz, 2005, Fresnel volume migration of multicomponent data: Geophysics, **70**, no. 6, S121–S129, https://doi.org/10.1190/1.2127114.

Reshetnikov, A., J. Kummerow, H. Asanuma, M. Häring, and S. A. Shapiro, 2015, Microseismic reflection imaging and its application to the Basel geothermal reservoir: Geophysics, **80**, no. 6, WC39–WC49, https://doi.org/10.1190/geo2014-0593.1.

Reshetnikov, A., J. Kummerow, S. Buske, and S. A. Shapiro, 2010, Microseismic imaging from a single geophone: KTB: 80th Annual International Meeting, SEG, Expanded Abstracts, 2070–2074, https://doi.org/10.1190/1.3513252.

Rutledge, J., and N. Soma, 2013, Using reflected phases to improve depth resolution of microseismic source locations from single-well observations: Unconventional Resources Technology Conference, Extended Abstracts, 208–217, https://doi.org/10.1190/urtec2013-024.

Vermeer, G. J. O., 2012, 3D seismic survey design, 2nd ed.: SEG, Geophysical references series, no. 12, https://doi.org/10.1190/1.9781560803041.

Wang, D., 2004, Vector 3C3D VSP Kirchhoff migration: 74th Annual International Meeting, SEG, Expanded Abstracts, 2458–2461, https://doi.org/10.1190/1.1851246.

Yang, Y., M. Zoback, M. Simon, and T. Dohmen, 2013, An integrated geomechanical and microseismic study of multi-well hydraulic fracture stimulation in the Bakken Formation: Unconventional Resources Technology Conference, Extended Abstracts, 534–543, https://doi.org/10.1190/urtec2013-056.

Zhu, T., and J. Sun, 2016, Data-driven diffraction imaging of fractures using passive seismic data: 86th Annual International Meeting, SEG, Expanded Abstracts, 2679–2683, https://doi.org/10.1190/segam2016-13845182.1.